Computing enhancement of the nonlinear $\mathrm{SP_N}$ approximations of radiative heat transfer in participating material

Youssef Belhamadia[1], Mohammed Seaid[2]

Abstract

Anisotropic mesh adaptation is an efficient procedure for controlling the output error of finite element simulations, particularly when used for three-dimensional problems. In this paper, we present an enhanced computational algorithm based on an anisotropic mesh adaptation for nonlinear $\mathrm{SP_N}$ approximations of radiative heat transfer in both two- and three-dimensional enclosures. Using an asymptotic analysis for the optical scale in the radiative transfer, the integro-differential equation is replaced by a series of partial differential equations of elliptic type. The nonlinear coupling between the heat transfer and radiation in the $\mathrm{SP_N}$ equations does not depend on the direction ordinates. In an anisotropic participating media, internal boundary layers with different magnitudes occur for each direction and developing an efficient numerical algorithm to accurately resolve them is a challenging task. In the present study, we propose an adaptive finite element method using an efficient hierarchical error estimator. A second-order scheme is used for the time integration and a Newton-type solver is implemented for the fully coupled nonlinear system. The proposed method has the potential to use large timesteps in the simulations for radiative heat transfer in anisotropic media at high temperatures. To demonstrate the viability of the method, several examples are presented for two- and three-dimensional problems. The numerical results confirm the capability of the proposed method to efficiently solve the nonlinear $\mathrm{SP_N}$ approximations of radiative transfer in anisotropic media.

Keywords: Radiative heat transfer; $\mathrm{SP_N}$ approximations; Anisotropic mesh adaptation; Finite element method; Three-dimensional nonlinear heat conduction

1 Introduction

Radiative heat transfer occurs in almost all industrial applications that involve high temperatures, such as glass manufacturing, industrial furnaces, gas turbine combustion chambers among others. In this type of applications, the radiation cannot be neglected and may even greatly influence the thermal features. From a mathematical point of view, the full radiative heat transfer model consists of a set of integro-differential equations that are spatially, spectrally, and directionally dependent. These equations are therefore extremely difficult to solve, especially when coupled with the energy transport equation. This complexity makes the numerical simulation complicated and computationally expensive. Therefore, the development of fast and accurate numerical algorithms for radiative heat transfer equations is critical and is needed in order to produce large scale numerical simulations. The physical and mathematical descriptions of full radiative heat transfer equations can be found for instance in [1, 2, 3]. To overcome some of the difficulties in solving these equations, several methods have been developed in the literature. The zonal and Monte-Carlo methods [1] are considered among the most accurate procedures developed for the radiative equation. However, these methods require large

---

[1] American University of Sharjah, Department of Mathematics and Statistics, Sharjah, United Arab Emirates. *E-mail:* ybelhamadia@aus.edu

[2] Department of Engineering, University of Durham, South Road, Durham DH1 3LE, United Kingdom. *E-mail:* m.seaid@durham.ac.uk

computational and storage requirements and they are limited when coupled with tools from the computational fluid dynamics. Similarly, the discrete ordinates method [4] is a suitable method for analysis of radiative heat transfer in practical engineering systems. However, this method still requires solving large systems of algebraic equations. Several other approaches have been developed to reduce the full radiative heat transfer model to a simpler form. These approaches include the Rosseland diffusion approximation [5, 6], the spherical harmonics method ($\mathrm{P_N}$) [7, 8, 9] and the simplified spherical harmonics method ($\mathrm{SP_N}$) [10, 11, 12, 13]. Although the $\mathrm{SP_N}$ models perform very well, especially when the medium is isotropic and optically thick, numerical simulations of these models are still challenging. In the literature, several numerical techniques have been developed to overcome some of these challenges. For instance, enriched partition of unity finite element methods have been implemented to solve the $\mathrm{SP_N}$ models in [14, 15]. Compared to the conventional finite element methods, these techniques have shown a significant gain in the computational time. However, they still require further study and enrichment adjustments for more advanced problems.

Adaptive methods were also developed to improve the accuracy of the numerical simulation and to capture the main radiative features in many contributions in the literature. In [13], a fully adaptive approach based on local refinements was presented to solve the $\mathrm{SP_N}$ approximation. In [16], a goal-oriented mesh adaptivity was proposed for the numerical solution of the multi-group $\mathrm{SP_N}$ equations. Although the approach required the solution of a dual problem, results presented have shown the benefits of this class of adaptive methods for solving the $\mathrm{SP_N}$ models. In [17], applications of *h*-, *p*-, and *hp*-mesh adaptation techniques have also been investigated for solving the $\mathrm{SP_3}$ equations. In [18], a class of *hp*-adaptive discontinuous Galerkin methods for solving the $\mathrm{SP_N}$ model in non-gray semi-transparent media was studied. It should also be stressed that adaptive methods have been widely investigated, not only for the $\mathrm{SP_N}$ models, but also for the full radiative model. For instance, a posteriori error estimates for a radiative transfer model have been analyzed in [19]. The approach is based on a suitable duality argument that guarantees a reliable error control. In [20], an Adaptive Mesh Refinement (AMR) algorithm has been implemented for the radiative transport equation. Furthermore, a cell-based AMR computations has been presented in [21] for solutions of the two-dimensional radiation transport problems, where both the goal-oriented AMR and the standard AMR techniques have been implemented. Recently, in [**?**] low-memory numerical methods based on hp-adaptive mesh refinements have been presented for the time-independent radiative transfer equation. However, in all above mentioned references, only structured computational meshes were employed accounting only for refinement, coarsening, and isotropic cells, which still limit the performance in the computational time and memory requirements. One way to overcome the difficulties of the above mentioned adaptive methods is to consider an anisotropic mesh adaptation. This adaptivity method increases the accuracy of simulations by considering spatial elements elongated along appropriate directions and it further minimizes the computational resources by reducing the total number of elements in the simulations. This technique has been successfully applied in many applications such as electrocardiology [22, 23, 24], computational fluid dynamics [25, 26, 27], phase change [28, 29], among others. To the best of our knowledge, the two- and three-dimensional anisotropic mesh adaptation techniques are not yet introduced for the radiative heat transfer problems, which is one of the objectives of this work.

In this work, we consider the nonlinear simplified approximations of radiative heat transfer in an anisotropic participating media for both two- and three-dimensional enclosures. Unlike the models investigated in [10, 11, 12, 13] for which the thermal properties are assumed to be constant, the $\mathrm{SP_N}$ models considered here account for nonlinear coefficient depending on the temperature of the medium. This assumption occurs in many physical applications since at high temperature, the thermal conductivity becomes nonlinear and it depends on the temperature. In addition, anisotropy of the medium is also accounted for in the present work allowing for the diffusion coefficient in the $\mathrm{SP_N}$ equations to be a full tensor depending on a rotation matrix for the directions. Another novelty in the current work consists of a fully coupled finite element formulation for the $\mathrm{SP_N}$ models where the equations are solved monolithically. This was not the case for most numerical methods developed in the literature for solving simplified approximations of radiative heat transfer, see [14, 13, 15]. A second-order accuracy in space using quadratic triangular and tetrahedral elements is implemented along with a fully implicit second-order Gear-based scheme in time. To deal with the non-linearity in the resulting system of equations, Newton's method is implemented which provides an additional advantage related to the selection of time-steps. To enhance the accuracy of the numerical solutions, a time-dependent mesh adaptation algorithm is developed as well. The technique is based on an hierarchical error estimator appropriate for second or higher order numerical solutions. Two- and three-dimensional problems are considered to show the effectiveness of the overall methodology. Comparison of the obtained results to those obtained using the full radiative heat transfer equations is also presented. The presented numerical results clearly show the capability of the proposed method to efficiently solve the nonlinear $\mathrm{SP_N}$ models in anisotropic media.

The present paper is organized as follows. The nonlinear $\mathrm{SP_N}$ approximations considered in this study are presented in section 2. Section 3 is devoted to the formulation of the finite element method for the $\mathrm{SP_N}$ models. This section includes the discretization and the anisotropic mesh adaptation. In section 4, we present numerical examples and results for the $\mathrm{SP_N}$ approximations of two- and three-dimensional radiative heat transfer at different optical regimes. Finally the conclusion is presented in section 5.

2 Nonlinear $\mathrm{SP_N}$ approximations of radiative heat transfer

In general, modelling radiative heat transfer requires integro-differential equations that depend on the space and direction due to the transport by photons, see for instance [1, 12, 13]. The model consists of a heat conduction equation for the temperature $\Theta(\boldsymbol{x},t)$ and a transport equation for the radiative intensity $I(\boldsymbol{x},\boldsymbol{s})$. These equations are reformulated in a dimensionless form as

$$\left\{\begin{array}{rcll}
\varepsilon^2\dfrac{\partial\Theta}{\partial t}-\varepsilon^2\nabla\cdot\big(\boldsymbol{K}\nabla\Theta\big) & = & -\kappa\left(4\pi B(\Theta)-\displaystyle\int_{\mathbb{S}^2} I(\boldsymbol{x},\boldsymbol{s})d\boldsymbol{s}\right), & (\boldsymbol{x},t)\in\mathcal{D}\times[0,T],\\
\varepsilon\boldsymbol{s}\cdot\nabla I+(\kappa+\sigma)I & = & \dfrac{\sigma}{4\pi}\displaystyle\int_{\mathbb{S}^2} I(\boldsymbol{x},\boldsymbol{s})d\boldsymbol{s}+\kappa B(\Theta), & (\boldsymbol{x},\boldsymbol{s})\in\mathcal{D}\times\mathbb{S}^2,\\
\varepsilon\boldsymbol{n}(\hat{\boldsymbol{x}})\cdot\boldsymbol{K}\nabla\Theta+h_c(\Theta-\Theta_b) & = & \alpha\pi\Big(B(\Theta_b)-B(\Theta)\Big), & (\hat{\boldsymbol{x}},t)\in\partial\mathcal{D}\times[0,T],\\
I(\hat{\boldsymbol{x}},\boldsymbol{s}) & = & B(\Theta_b), & (\hat{\boldsymbol{x}},\boldsymbol{s})\in\partial\mathcal{D}^-\times\mathbb{S}^2,\\
\Theta(\boldsymbol{x},0) & = & \Theta_0(\boldsymbol{x}), & \boldsymbol{x}\in\mathcal{D},
\end{array}\right. \tag{2.1}$$

where $\mathcal{D}\subset\mathbb{R}^d$ ($d=2$ or 3) is a geometrical domain with a boundary $\partial\mathcal{D}$ of an absorbing and emitting semi-transparent material, $[0,T]$ is the time interval, $I(\boldsymbol{x},\boldsymbol{s})$ is the spectral intensity at the point $\boldsymbol{x}$ and with the propagation direction $\boldsymbol{s}$. Here, $\boldsymbol{K}$ is the thermal conductivity, κ the absorption coefficient, h_c the convective heat transfer coefficient, σ the scattering coefficient, Θ_b a given ambient temperature of the surrounding, Θ_0 a given initial temperature of the media, $\mathbb{S}^2$ denotes the unit sphere, $\boldsymbol{n}(\hat{\boldsymbol{x}})$ the outward normal at $\hat{\boldsymbol{x}}$ to the boundary $\partial\mathcal{D}$, α the mean hemispheric surface emissivity, $\varepsilon\in(0,1]$ is a diffusion scale. In (2.1), the spectral intensity of the black-body radiation, $B(\Theta)$, is defined as

$$B(\Theta)=a_R\Theta^4, \tag{2.2}$$

where a_R is the Stefan-Boltzmann constant, see for instance [1]. Note that on the boundary we consider the transmitting and specular reflecting conditions where the boundary region $\partial\mathcal{D}^-$ in (2.1) is defined as

$$\partial\mathcal{D}^-=\Big\{\hat{\boldsymbol{x}}\in\partial\mathcal{D}:\quad \boldsymbol{n}(\hat{\boldsymbol{x}})\cdot\boldsymbol{s}<0\Big\}.$$

More details on modelling radiative heat transfer in semitransparent media can be found in [1, 30] among others. In addition, details on the passage from dimensional equations to the dimensionless system (2.1) can be found in [13, 12] and for brevity in the presentation are not repeated here. Obviously, when the absorption coefficient $\kappa=0$, the heat conduction and the radiative transfer equations in (2.1) become decoupled and physically no radiation is accounted for in the temperature distribution. Therefore, only positive absorption coefficients ($\kappa\neq 0$) are considered in the present study.

In this section, we briefly show how to reformulate the radiative heat transfer equations (2.1) using the $\mathrm{SP_N}$ approximations. For more details, the reader is referred to [12] and the references therein. Thus, we rewrite the radiative transfer equation in (2.1) as

$$\left(1+\frac{\varepsilon}{\kappa+\sigma}\boldsymbol{s}\cdot\nabla\right)I=Q, \tag{2.3}$$

where the source term Q is defined by

$$Q=\frac{\sigma}{4\pi\left(\kappa+\sigma\right)}\varphi+\frac{\kappa}{\kappa+\sigma}B(\Theta), \qquad \text{with} \qquad \varphi=\int_{\mathbb{S}^2}I(\boldsymbol{x},\boldsymbol{s})d\boldsymbol{s}.$$

Next, we formally invert the transport operator in (2.3) using the Neumann series as follows

$$\begin{aligned} I &= \left(1+\frac{\varepsilon}{\kappa+\sigma}\boldsymbol{s}\cdot\nabla\right)^{-1}Q, \\ &\approx \left(1-\frac{\varepsilon}{\kappa+\sigma}\boldsymbol{s}\cdot\nabla+\frac{\varepsilon^2}{\left(\kappa+\sigma\right)^2}\left(\boldsymbol{s}\cdot\nabla\right)^2-\frac{\varepsilon^3}{\left(\kappa+\sigma\right)^3}\left(\boldsymbol{s}\cdot\nabla\right)^3+\frac{\varepsilon^4}{\left(\kappa+\sigma\right)^4}\left(\boldsymbol{s}\cdot\nabla\right)^4+\ldots\right)Q. \end{aligned} \tag{2.4}$$

The expansion (2.4) is then integrated with respect to $\boldsymbol{s}$ over all directions in the unit sphere S^2 and by using the well-established relation

$$\int_{S^2}\left(\boldsymbol{s}\cdot\nabla\right)^n d\boldsymbol{s}=\Big(1+(-1)^n\Big)\frac{2\pi}{n+1}\nabla^n, \qquad n=1,2,\ldots.$$

the formal asymptotic equation for the mean intensity φ is hence given by

$$4\pi Q=\left(1-\frac{\varepsilon^2}{3\left(\kappa+\sigma\right)^2}\nabla^2-\frac{4\varepsilon^4}{45\left(\kappa+\sigma\right)^4}\nabla^4-\frac{44\varepsilon^6}{94\left(\kappa+\sigma\right)^6}\nabla^6\right)\varphi+\mathcal{O}(\varepsilon^8).$$

Now the $\mathrm{SP_0}$, $\mathrm{SP_1}$, $\mathrm{SP_2}$ or $\mathrm{SP_3}$ approximations are obtained by neglecting the terms of order $\mathcal{O}(\varepsilon^2)$, $\mathcal{O}(\varepsilon^4)$, $\mathcal{O}(\varepsilon^6)$ or $\mathcal{O}(\varepsilon^8)$, respectively. In the present study, we consider only the $\mathrm{SP_1}$ and $\mathrm{SP_3}$ approximations but our anisotropic mesh adaptation can easily be extended to other $\mathrm{SP_N}$ approximations. The $\mathrm{SP_1}$ and $\mathrm{SP_3}$ approximations can now be briefly presented but for more details the reader is referred to [12].

For the $\mathrm{SP_1}$ approximation:

$$4\pi Q=\varphi-\frac{\varepsilon^2}{3\left(\kappa+\sigma\right)^2}\nabla^2\varphi+\mathcal{O}(\varepsilon^4),$$

and the $\mathrm{SP_1}$ model reads

$$\begin{aligned} -\nabla\cdot\left(\frac{\varepsilon^2}{3\left(\kappa+\sigma\right)}\nabla\varphi\right)+\kappa\varphi &= 4\pi\kappa B(\Theta), && \boldsymbol{x}\in\mathcal{D}, \\ \varphi+\left(\frac{2\varepsilon}{3\left(\kappa+\sigma\right)}\right)\boldsymbol{n}(\hat{\boldsymbol{x}})\cdot\nabla\varphi &= 4\pi B(\Theta_b), && \hat{\boldsymbol{x}}\in\partial\mathcal{D}. \end{aligned} \tag{2.5}$$

For the $\mathrm{SP_3}$ approximation:

$$4\pi Q=\left(1-\frac{\varepsilon^2}{3\left(\kappa+\sigma\right)^2}\nabla^2-\frac{4\varepsilon^4}{45\left(\kappa+\sigma\right)^4}\nabla^4-\frac{44\varepsilon^6}{94\left(\kappa+\sigma\right)^6}\nabla^6\right)\varphi+\mathcal{O}(\varepsilon^8),$$

and the $\mathrm{SP_3}$ model is defined as

$$\begin{aligned} -\nabla\cdot\left(\frac{\varepsilon^2\mu_1^2}{3\left(\kappa+\sigma\right)}\nabla\varphi_1\right)+\kappa\varphi_1 &= 4\pi\kappa B(\Theta), && \boldsymbol{x}\in\mathcal{D}, \\ -\nabla\cdot\left(\frac{\varepsilon^2\mu_2^2}{3\left(\kappa+\sigma\right)}\nabla\varphi_2\right)+\kappa\varphi_2 &= 4\pi\kappa B(\Theta), && \boldsymbol{x}\in\mathcal{D}, \\ \alpha_1\varphi_1+\frac{\varepsilon}{\kappa+\sigma}\boldsymbol{n}(\hat{\boldsymbol{x}})\cdot\nabla\varphi_1 &= -\beta_2\varphi_2+\eta_1 B(\Theta_b),, && \hat{\boldsymbol{x}}\in\partial\mathcal{D}, \\ \alpha_2\varphi_2+\frac{\varepsilon}{\kappa+\sigma}\boldsymbol{n}(\hat{\boldsymbol{x}})\cdot\nabla\varphi_2 &= -\beta_1\varphi_1+\eta_2 B(\Theta_b), && \hat{\boldsymbol{x}}\in\partial\mathcal{D}. \end{aligned} \tag{2.6}$$

The mean radiative intensity φ is calculated from the variables φ_1 and φ_2 as

$$\varphi = \frac{\gamma_2\varphi_1 - \gamma_1\varphi_2}{\gamma_2 - \gamma_1}.$$

and the other constants are as follow:

$$\mu_1^2 = \frac{3}{7}\left(3 - 2\sqrt{\frac{6}{5}}\right), \quad \mu_2^2 = \frac{3}{7}\left(3 + 2\sqrt{\frac{6}{5}}\right), \quad \gamma_1 = \frac{5}{7}\left(1 - 3\sqrt{\frac{6}{5}}\right), \quad \gamma_2 = \frac{5}{7}\left(1 + 3\sqrt{\frac{6}{5}}\right),$$

$$\begin{array}{lll} \alpha_1 = \dfrac{C_1D_4 - C_4D_1}{C_3D_4 - D_3C_4}, & \eta_1 = \dfrac{D_4\rho_1 - C_4\rho_3}{C_3D_4 - D_3C_4}, & \beta_1 = \dfrac{C_3D_1 - C_1D_3}{C_3D_4 - D_3C_4}, \\ \alpha_2 = \dfrac{C_3D_2 - C_2D_3}{C_3D_4 - D_3C_4}, & \eta_2 = \dfrac{C_3\rho_3 - D_3\rho_1}{C_3D_4 - D_3C_4}, & \beta_2 = \dfrac{C_2D_4 - C_4D_2}{C_3D_4 - D_3C_4}, \end{array}$$

where

$$\begin{array}{llll} A_1 = \dfrac{1}{4}, & B_1 = -\dfrac{1}{16}, & C_1 = w_0(\gamma_2A_1 - A_2), & D_1 = w_0(\gamma_2B_1 - B_2), \\ A_2 = \dfrac{5}{16}, & B_2 = \dfrac{5}{16}, & C_2 = w_0(-\gamma_1A_1 + A_2), & D_2 = w_0(-\gamma_1B_1 + B_2), \\ A_3 = \dfrac{1}{6}, & B_3 = \dfrac{3r_4}{6}, & C_3 = w_0(\gamma_2A_3 - A_4), & D_3 = w_0(\gamma_2B_3 - B_4), \\ A_4 = \dfrac{2}{9}, & B_4 = \dfrac{3}{14}, & C_4 = w_0(-\gamma_1A_3 - A_4), & D_4 = w_0(-\gamma_1B_3 + B_4), \end{array}$$

with

$$w_0 = \frac{7}{36}\sqrt{\frac{6}{5}}, \qquad \rho_1 = \pi, \qquad \rho_3 = -\frac{\pi}{4}.$$

Note that these parameters do not depend on the space dimensions of the problem under study and their existence has been derived from the asymptotic analysis reported in [12]. In our simulations presented in this study, these parameters are assumed to be constant, calculated in advance and stored to be used whenever a simulation of solution has to be repeated in the time loop.

3 Anisotropic mesh adaptation finite element method

In the current study, we are interested in radiative heat transfer in heterogeneous anisotropic media for which the conductivity, absorption and scattering processes depend on the direction and the spatial location. We also assume that the thermal conductivity depends on the temperature in a nonlinear manner. In these cases, the SP_1 model for the heterogeneous and anisotropic media becomes

$$\left\{ \begin{array}{rcll} \varepsilon^2\dfrac{\partial\Theta}{\partial t} - \varepsilon^2\nabla\cdot\big(\boldsymbol{K}\nabla\Theta\big) & = & -\kappa\big(4\pi B(\Theta) - \varphi\big), & (\boldsymbol{x}, t) \in \mathcal{D}\times[0, T], \\ -\varepsilon^2\nabla\cdot\big(\boldsymbol{\mathcal{E}}\nabla\varphi\big) + \kappa\varphi & = & 4\pi\kappa B(\Theta), & (\boldsymbol{x}, t) \in \mathcal{D}\times[0, T], \\ \varepsilon\boldsymbol{K}\nabla\Theta\cdot\boldsymbol{n}(\hat{\boldsymbol{x}}) + h_c(\Theta - \Theta_b) & = & \alpha\pi\Big(B(\Theta_b) - B(\Theta)\Big), & (\hat{\boldsymbol{x}}, t) \in \partial\mathcal{D}\times[0, T], \\ \varepsilon^2\boldsymbol{\mathcal{E}}\nabla\varphi\cdot\boldsymbol{n}(\hat{\boldsymbol{x}}) + \dfrac{\varepsilon}{2}\varphi & = & \dfrac{\varepsilon}{2}4\pi B(\Theta_b), & (\hat{\boldsymbol{x}}, t) \in \partial\mathcal{D}\times[0, T], \\ \Theta(\boldsymbol{x}, 0) & = & \Theta_0(\boldsymbol{x}), & \boldsymbol{x} \in \mathcal{D}, \end{array} \right. \tag{3.1}$$

where for the two-dimensional problems,

$$\boldsymbol{K} = \boldsymbol{\mathcal{R}}(\theta)\begin{pmatrix} K_{11}(\Theta) & 0 \\ 0 & K_{22}(\Theta)\end{pmatrix}\boldsymbol{\mathcal{R}}^{-1}(\theta), \qquad \boldsymbol{\mathcal{E}} = \begin{pmatrix} \dfrac{1}{3\,(\kappa+\sigma)} & 0 \\ 0 & \dfrac{1}{3\,(\kappa+\sigma)}\end{pmatrix},$$

with $\boldsymbol{\mathcal{R}}(\theta)$ is the rotation matrix given by

$$\boldsymbol{\mathcal{R}}(\theta) = \begin{pmatrix} \cos\theta & -\sin\theta \\ \sin\theta & \cos\theta \end{pmatrix}. \tag{3.2}$$

It should be stressed that the anisotropy in (3.1) comes from the fact that the conductivity coefficient does not depend on the location only but it also depends on the direction defined by the angle θ in (3.2), see for example [31, 32]. For the three-dimensional case, these tensors are defined as

$$\boldsymbol{K} = \boldsymbol{\mathcal{R}}(\theta)\begin{pmatrix} K_{11}(\Theta) & 0 & 0 \\ 0 & K_{22}(\Theta) & 0 \\ 0 & 0 & K_{11}(\Theta)\end{pmatrix}\boldsymbol{\mathcal{R}}^{-1}(\theta), \quad \boldsymbol{\mathcal{E}} = \begin{pmatrix} \dfrac{1}{3\,(\kappa+\sigma)} & 0 & 0 \\ 0 & \dfrac{1}{3\,(\kappa+\sigma)} & 0 \\ 0 & 0 & \dfrac{1}{3\,(\kappa+\sigma)}\end{pmatrix},$$

where $\boldsymbol{\mathcal{R}}(\theta)$ is the three-dimensional rotation matrix given by

$$\boldsymbol{\mathcal{R}}(\theta) = \begin{pmatrix} 1 & 0 & 0 \\ 0 & \cos\theta & -\sin\theta \\ 0 & \sin\theta & \cos\theta \end{pmatrix}. \tag{3.3}$$

Similarly, the SP$_3$ equations for the heterogeneous and anisotropic media are defined as

$$\left\{\begin{array}{rcll} \varepsilon^2\dfrac{\partial\Theta}{\partial t} - \varepsilon^2\nabla\cdot\big(\boldsymbol{K}\nabla\Theta\big) & = & -\kappa\left(4\pi B(\Theta) - \dfrac{\gamma_2\varphi_1-\gamma_1\varphi_2}{\gamma_2-\gamma_1}\right), & (\boldsymbol{x},t)\in\mathcal{D}\times[0,T], \\ -\varepsilon^2\mu_1^2\nabla\cdot\big(\boldsymbol{\mathcal{E}}\nabla\varphi_1\big) + \kappa\varphi_1 & = & 4\pi\kappa B(\Theta), & (\boldsymbol{x},t)\in\mathcal{D}\times[0,T], \\ -\varepsilon^2\mu_2^2\nabla\cdot\big(\boldsymbol{\mathcal{E}}\nabla\varphi_2\big) + \kappa\varphi_2 & = & 4\pi\kappa B(\Theta), & (\boldsymbol{x},t)\in\mathcal{D}\times[0,T], \\ \varepsilon\boldsymbol{K}\nabla\Theta\cdot\boldsymbol{n}(\hat{\boldsymbol{x}}) + h_c(\Theta-\Theta_b) & = & \alpha\pi\Big(B(\Theta_b)-B(\Theta)\Big), & (\hat{\boldsymbol{x}},t)\in\partial\mathcal{D}\times[0,T], \\ \varepsilon^2\mu_1^2\boldsymbol{\mathcal{E}}\nabla\varphi_1\cdot\boldsymbol{n}(\hat{\boldsymbol{x}}) + \dfrac{\varepsilon\mu_1^2\alpha_1}{3}\varphi_1 & = & -\dfrac{\varepsilon\mu_1^2\beta_2}{3}\varphi_2 + \dfrac{\varepsilon\mu_1^2\eta_1}{3}B(\Theta_b), & (\hat{\boldsymbol{x}},t)\in\partial\mathcal{D}\times[0,T], \\ \varepsilon^2\mu_2^2\boldsymbol{\mathcal{E}}\nabla\varphi_2\cdot\boldsymbol{n}(\hat{\boldsymbol{x}}) + \dfrac{\varepsilon\mu_2^2\alpha_2}{3}\varphi_2 & = & -\dfrac{\varepsilon\mu_2^2\beta_1}{3}\varphi_1 + \dfrac{\varepsilon\mu_2^2\eta_2}{3}B(\Theta_b), & (\hat{\boldsymbol{x}},t)\in\partial\mathcal{D}\times[0,T], \\ \Theta(\boldsymbol{x},0) & = & \Theta_0(\boldsymbol{x}), & \boldsymbol{x}\in\mathcal{D}. \end{array}\right. \tag{3.4}$$

Note that by setting $\theta = 0$ in the above equations, the systems (3.1) and (3.4) reduce to the conventional SP$_1$ and SP$_3$ approximations (2.5) and (2.6), respectively. In this paper, we formulate our anisotropic mesh adaptation finite element method for solving both SP$_1$ (3.1) and SP$_3$ (3.4) approximations. Few words on the coercivity of the matrices .....

3.1 Finite element discretization

Unlike many numerical methods developed in the literature such as [33, 12, 34, 35, 36, 13], the SP_3 equations (3.4) are solved monolithically instead of solving them separately, where the equations are decoupled. In the present study, to integrate the equations (3.1) and (3.4) in time we consider a second-order implicit scheme of Gear type also known in the literature by backward differentiation formula (BDF2). For the space discretization, we implement a finite element method using quadratic triangular and tetrahedral elements on unstructured meshes. Here, the time interval is also divided into sub-intervals $[t_n, t_{n+1}]$ with uniform length $\Delta t = t_{n+1} - t_n$ for $n = 0, 1, \ldots$. We use the notation $w^n := w(\boldsymbol{x}, t_n)$ to denote the value of a generic function w at time t_n. Hence, using ψ as the test functions, the discrete weak form of the SP_1 system (3.1) reads as: Find $\left(\Theta^{n+1}, \varphi^{n+1}\right) \in V_h^0 \times V_h^0$, such that

$$\begin{aligned}
\int_{\mathcal{D}} \frac{3\Theta^{n+1} - 4\Theta^n + \Theta^{n-1}}{2\Delta t} \psi \, d\mathcal{D} + \int_{\mathcal{D}} \mathbf{K} \nabla \Theta^{n+1} \cdot \nabla \psi \, d\mathcal{D} &= \int_{\mathcal{D}} \frac{\kappa}{\varepsilon^2} \Big(\varphi^{n+1} - 4\pi B\left(\Theta^{(n+1)}\right) \Big) \psi \, d\mathcal{D} + \\
&\quad \int_{\partial\mathcal{D}} \left(\frac{h_c}{\varepsilon} \left(\Theta_b - \Theta^{n+1} \right) + \frac{\alpha\pi}{\varepsilon} \Big(B(\Theta_b) - B\left(\Theta^{n+1}\right) \Big) \right) \psi \, d\mathcal{D}, \\
\varepsilon^2 \int_{\mathcal{D}} \boldsymbol{\mathcal{E}} \nabla \varphi^{n+1} \cdot \nabla \psi \, d\mathcal{D} + \int_{\mathcal{D}} \kappa \varphi^{n+1} \psi \, d\mathcal{D} &= \int_{\mathcal{D}} 4\pi\kappa B\left(\Theta^{n+1}\right) \psi \, d\mathcal{D} + \int_{\partial\mathcal{D}} \frac{\varepsilon}{2} \Big(4\pi B(\Theta_b) - \varphi^{n+1} \Big) \psi \, d\mathcal{D}.
\end{aligned} \tag{3.5}$$

Similarly, the discrete weak form of the SP_3 system (3.4) reads as: Find $\left(\Theta^{n+1}, \varphi_1^{n+1}, \varphi_2^{n+1}\right) \in V_h^0 \times V_h^0 \times V_h^0$, such that

$$\begin{aligned}
\int_{\mathcal{D}} \frac{3\Theta^{n+1} - 4\Theta^n + \Theta^{n-1}}{2\Delta t} \psi \, d\mathcal{D} + \int_{\mathcal{D}} \mathbf{K} \nabla \Theta^{n+1} \cdot \nabla \psi \, d\mathcal{D} &= \int_{\mathcal{D}} \frac{\kappa}{\varepsilon^2} \left(\frac{\gamma_2 \varphi_1^{n+1} - \gamma_1 \varphi_2^{n+1}}{\gamma_2 - \gamma_1} - 4\pi B\left(\Theta^{n+1}\right) \right) \psi \, d\mathcal{D} + \\
&\quad \int_{\partial\mathcal{D}} \left(\frac{h_c}{\varepsilon} \left(\Theta_b - \Theta^{n+1} \right) + \frac{\alpha\pi}{\varepsilon} \Big(B(\Theta_b) - B\left(\Theta^{n+1}\right) \Big) \right) \psi \, d\mathcal{D}, \\
\varepsilon^2 \mu_1^2 \int_{\mathcal{D}} \boldsymbol{\mathcal{E}} \nabla \varphi_1^{n+1} \cdot \nabla \psi \, d\mathcal{D} + \int_{\mathcal{D}} \kappa \varphi_1^{n+1} \psi \, d\mathcal{D} &= \int_{\mathcal{D}} 4\pi\kappa B\left(\Theta^{n+1}\right) \psi \, d\mathcal{D} + \\
&\quad \int_{\partial\mathcal{D}} \frac{\varepsilon \mu_1^2}{3} \Big(\eta_1 B(\Theta_b) - \beta_2 \varphi_2^{n+1} - \alpha_1 \varphi_1^{n+1} \Big) \psi \, d\mathcal{D}, \\
\varepsilon^2 \mu_2^2 \int_{\mathcal{D}} \boldsymbol{\mathcal{E}} \nabla \varphi_2^{n+1} \cdot \nabla \psi \, d\mathcal{D} + \int_{\mathcal{D}} \kappa \varphi_2^{n+1} \psi \, d\mathcal{D} &= \int_{\mathcal{D}} 4\pi\kappa B\left(\Theta^{n+1}\right) \psi \, d\mathcal{D} + \\
&\quad + \int_{\partial\mathcal{D}} \frac{\varepsilon \mu_2^2}{3} \Big(\eta_2 B(\Theta_b) - \beta_1 \varphi_1^{n+1} - \alpha_2 \varphi_2^{n+1} \Big) \psi \, d\mathcal{D},
\end{aligned} \tag{3.6}$$

where $V_h^0 = V_h \cap H_0^1(\mathcal{D})$ and V_h is defined by

$$V_h = \Big\{ w_h \in C^0(\mathcal{D}) : \quad w_h \Big|_T \in \mathbb{P}_p(T), \quad \forall\, T \in \mathcal{T}_h \Big\}. \tag{3.7}$$

In general, other time stepping schemes can also be used for the SP_N models. However, we consider the BDF2 method in this study as this scheme provided better numerical solutions compared to other first- and second-order schemes in our previous work [37] and highly accurate solutions in different other type of applications, see for example [38, 39]. Notice that, when using the BDF2 scheme, a simple backward Euler scheme or Crank-Nicolson method can be used to compute the solution at the first time step.

In the current study, the Newton's method is used at each timestep to solve the nonlinear systems (3.5) and (3.6). For the SP_3 model, we start with the triplet $\left(\Theta_0^{n+1}, {\varphi_1}_0^{n+1}, {\varphi_2}_0^{n+1}\right) = \left(\Theta^n, {\varphi_1}^n, {\varphi_2}^n\right)$ and we impose $\Theta_{k+1}^{n+1} = \Theta_k^{n+1} + \delta_\Theta$, ${\varphi_1}_{k+1}^{n+1} = {\varphi_1}_k^{n+1} + \delta_{\varphi_1}$, and ${\varphi_2}_{k+1}^{n+1} = {\varphi_2}_k^{n+1} + \delta_{\varphi_2}$. We linearize the nonlinear terms using the Taylor expansion as

$$B(\Theta_{k+1}^{n+1}) = B(\Theta_k^{n+1} + \delta_\Theta) \approx B(\Theta_k^{n+1}) + B'(\Theta_k^{n+1})\delta_\Theta,$$

where $B'(\Theta) = \dfrac{dB(\Theta)}{d\Theta}$. Then, the new linearized monolithic system of equations in terms of δ_Θ, δ_{φ_1}, and δ_{φ_2} for the SP$_3$ equations is given by

$$
\begin{aligned}
&\int_{\mathcal{D}} \frac{3\delta_\Theta}{2\Delta t}\psi \; d\mathcal{D} + \int_{\mathcal{D}} \mathbf{K}\nabla\delta_\Theta \cdot \nabla\psi \; d\mathcal{D} - \int_{\mathcal{D}} \frac{\kappa}{\varepsilon^2}\left(\frac{\gamma_2\delta_{\varphi_1} - \gamma_1\delta_{\varphi_2}}{\gamma_2 - \gamma_1} - 4\pi B'\left(\Theta_k^{n+1}\right)\delta_\Theta\right)\psi \; d\mathcal{D} + \\
&\qquad \int_{\partial\mathcal{D}} \Big(\frac{h_c}{\varepsilon} + \frac{\alpha\pi}{\varepsilon}B'(\Theta_k^{n+1})\Big)\delta_\Theta\psi \; d\mathcal{D} = -\int_{\mathcal{D}} \frac{3\Theta_k^{n+1} - 4\Theta^n + \Theta^{n-1}}{2\Delta t}\psi \; d\mathcal{D} - \int_{\mathcal{D}} \mathbf{K}\nabla\Theta_k^{n+1} \cdot \nabla\psi \; d\mathcal{D} + \\
&\int_{\mathcal{D}} \frac{\kappa}{\varepsilon^2}\left(\frac{\gamma_2\varphi 1_k^{n+1} - \gamma_1\varphi 2_k^{n+1}}{\gamma_2 - \gamma_1} - 4\pi B\left(\Theta_k^{n+1}\right)\right)\psi \; d\mathcal{D} + \int_{\partial\mathcal{D}}\left(\frac{h_c}{\varepsilon}\left(\Theta_b - \Theta_k^{n+1}\right) + \frac{\alpha\pi}{\varepsilon}\Big(B(\Theta_b) - B(\Theta_k^{n+1})\Big)\right)\psi \; d\mathcal{D}, \\
&\varepsilon^2\mu_1^2\int_{\mathcal{D}} \boldsymbol{\mathcal{E}}\nabla\delta_{\varphi_1} \cdot \nabla\psi \; d\mathcal{D} + \int_{\mathcal{D}} \kappa\delta_{\varphi_1}\psi \; d\mathcal{D} - \int_{\mathcal{D}} 4\pi\kappa B'(\Theta_k^{n+1})\delta_\Theta\psi \; d\mathcal{D} + \int_{\partial\mathcal{D}} \frac{\varepsilon\mu_1^2}{3}\Big(\beta_2\delta_{\varphi_2} + \alpha_1\delta_{\varphi_1}\Big)\psi \; d\mathcal{D} = \\
&\qquad -\varepsilon^2\mu_1^2\int_{\mathcal{D}} \boldsymbol{\mathcal{E}}\nabla\varphi 1_k^{n+1} \cdot \nabla\psi \; d\mathcal{D} - \int_{\mathcal{D}} \kappa\varphi 1_k^{n+1}\psi \; d\mathcal{D} + \int_{\mathcal{D}} 4\pi\kappa B(\Theta_k^{n+1})\psi \; d\mathcal{D} + \\
&\qquad \int_{\partial\mathcal{D}} \frac{\varepsilon\mu_1^2}{3}\Big(\eta_1 B(\Theta_b) - \beta_2\varphi 2_k^{n+1} - \alpha_1\varphi 1_k^{n+1}\Big)\psi \; d\mathcal{D}, \\
&\varepsilon^2\mu_2^2\int_{\mathcal{D}} \boldsymbol{\mathcal{E}}\nabla\delta_{\varphi_2} \cdot \nabla\psi \; d\mathcal{D} + \int_{\mathcal{D}} \kappa\delta_{\varphi_2}\psi \; d\mathcal{D} - \int_{\mathcal{D}} 4\pi\kappa B'(\Theta_k^{n+1})\delta_\Theta\psi \; d\mathcal{D} + \int_{\partial\mathcal{D}} \frac{\varepsilon\mu_2^2}{3}\Big(\beta_1\delta_{\varphi_1} + \alpha_2\delta_{\varphi_2}\Big)\psi \; d\mathcal{D} = \\
&\qquad -\varepsilon^2\mu_2^2\int_{\mathcal{D}} \boldsymbol{\mathcal{E}}\nabla\varphi 2_k^{n+1} \cdot \nabla\psi \; d\mathcal{D} - \int_{\mathcal{D}} \kappa\varphi 2_k^{n+1}\psi \; d\mathcal{D} + \int_{\mathcal{D}} 4\pi\kappa B(\Theta_k^{n+1})\psi \; d\mathcal{D} + \\
&\qquad \int_{\partial\mathcal{D}} \frac{\varepsilon\mu_2^2}{3}\Big(\eta_2 B(\Theta_b) - \beta_1\varphi 1_k^{n+1} - \alpha_2\varphi 2_k^{n+1}\Big)\psi \; d\mathcal{D}.
\end{aligned}
\tag{3.8}
$$

Similar idea can be used for the SP$_1$ model but it is not presented to avoid repetitions. Notice that following similar arguments as those reported in [40], the finite element matrices involved in (3.8) are positive semi-definite. It should also be noted that linear systems resulting from the Newton's method are solved by iterative methods. An incomplete *LU* decomposition (ILU) GMRES solver from the `PETSc`[1] library is used, see for example [41, 42]. The convergence of the Newton's iterations was achieved when the residual norm is less than 10^{-6}. Obviously, this convergence depends on the value taken by the time-step Δt but in all our calculations, three to five iterations were sufficient to achieve the required convergence.

3.2 Mesh adaptation procedure

In the current work, an adaptive method is implemented to improve the accuracy of the finite element solutions of the SP$_\text{N}$ models. The main goal of the adaptive method is to reduce the spatial mesh size as well as the computational cost while maintaining and even improving the accuracy of the computed solutions. Here, the adaptive technique is based on an error estimator applicable to second or higher order variables for both two- and three-dimensional cases. Details on this procedure are provided in [28, 29, 43, 44, 45] and the method is fairly general and can be employed in various applications. The error estimator is based on the construction of an enriched numerical solution. In fact, if we consider Θ as the unknown exact solution and $\Theta_h^{(k)}$ is its numerical approximation of degree k, the error can be bounded in some appropriate functional norms as follows

$$
\|\Theta - \Theta_h^{(k)}\| \leq \frac{1}{1-\beta}\|\hat{\Theta}_h^{(k+1)} - \Theta_h^{(k)}\|, \tag{3.9}
$$

where $\beta < 1$ and $\hat{\Theta}_h^{(k+1)}$ is the enriched solution of degree $k+1$ defined as

$$
\hat{\Theta}_h^{(k+1)} = \Theta_h^{(k)} + c_h^{(k+1)}.
$$

---

[1] http://www.mcs.anl.gov/petsc/

Algorithm 1: Steps used for solving the SP$_3$ model.

```
Assuming $\Theta^{n-1}$, $\Theta^n$, $\varphi_1^{n-1}$, $\varphi_1^n$, $\varphi_2^{n-1}$ and $\varphi_2^n$ are known in the mesh $\mathcal{M}^n$ at time $t_n$.
for $n = 1, \ldots,$ do
    Compute the approximations $\widetilde{\Theta}^{n+1}$, $\widetilde{\varphi_1}^{n+1}$ and $\widetilde{\varphi_2}^{n+1}$ at time $t^{n+1}$ by solving the system (3.8) on the mesh $\mathcal{M}^n$.
    Adapt the mesh to obtain a new mesh $\mathcal{M}^{(n+1)}$ starting from the mesh $\mathcal{M}^{(n)}$ and the approximations
        $\frac{\Theta^{(n-1)} + \Theta^{(n)} + \widetilde{\Theta}^{(n+1)}}{3}, \qquad \frac{\varphi_1^{(n)} + \widetilde{\varphi_1}^{(n+1)}}{2} \quad \text{and} \quad \frac{\varphi_2^{(n)} + \widetilde{\varphi_2}^{(n+1)}}{2}.$
    Reinterpolate $\Theta^{n-1}$, $\Theta^n$, $\varphi_1^{n-1}$, $\varphi_1^n$, $\varphi_2^{n-1}$ and $\varphi_2^n$ on the mesh $\mathcal{M}^{n+1}$.
    Compute $\Theta^{n+1}$, ${\varphi_1}^{n+1}$ and ${\varphi_2}^{n+1}$ by solving the system (3.8) on the mesh $\mathcal{M}^{(n+1)}$.
end for
```

Therefore, the error $\|\Theta - \Theta_h^{(k)}\|$ is clearly controlled by the correction $c_h^{(k+1)}$. The reconstruction of $c_h^{(k+1)}$ is based on an accurate evaluation of the gradient of $\Theta_h^{(k)}$ at the nodes. More details about the reconstruction of the enriched solution can be found in [45].

The anisotropic mesh adaptation procedure is then obtained by local operations on the mesh (edge refinement, edge swapping, vertex suppression and vertex displacement). More details about the local operations on the mesh can be found in [43]. Since the radiative heat transfer is a time-dependent problem, an algorithm that includes the above mentioned adaptive method needs to be presented to get an adapted mesh at each time-step. To avoid repetitions, we present in Algorithm 1 the main steps used for solving the SP$_3$ model only and the application to the SP$_1$ system can be carried out using similar steps.

4 Numerical results

To assess the accuracy and the reliability of the method proposed in this study, examples of radiative heat transfer in two- and three-dimensional enclosures are presented. In both two- and three-dimensional problems, comparisons between results obtained using the full radiative model and those obtained using the SP$_n$ models are presented for a test problem of radiative heat transfer in isotropic media along with other examples of radiative heat transfer in anisotropic media. Qualitative and quantitative results are presented showing the performance of our proposed methodology. In all our simulations presented in this section, the Planck function $B(\Theta)$ is defined by (2.2) with the Stefan-Boltzmann radiation constant $a_R = 5.67 \times 10^{-8}$. All the computations are performed on a Dell Precision 7920 Tower with 20C Dual Intel Xeon Gold 6148 2.4GHz processor and 64GB 2666MHz DDR4 Memory.

4.1 Radiative heat transfer in two-dimensional enclosures

To demonstrate the performance of the proposed method, we first solve the the SP$_1$ model (2.5) and SP$_3$ model (2.6) and compare the numerical results with those obtained with the full radiative heat transfer equations (2.1) at two different asymptotic limits corresponding to $\varepsilon = 1$ and $\varepsilon = 0.1$. Here, we consider the isotropic case with $\boldsymbol{K} = \mathbf{I}$, in unit square $\mathcal{D} = [0, 1] \times [0, 1]$ with the absorption coefficient $\kappa = 1$, the scattering coefficient $\sigma = 0$, the convective heat transfer coefficient $h_c = 1$ and the surface emissivity $\alpha = 0$. The initial and boundary temperatures are given as $\Theta_0 = 1500$ and $\Theta_b = 300$, respectively. The numerical results are performed using a

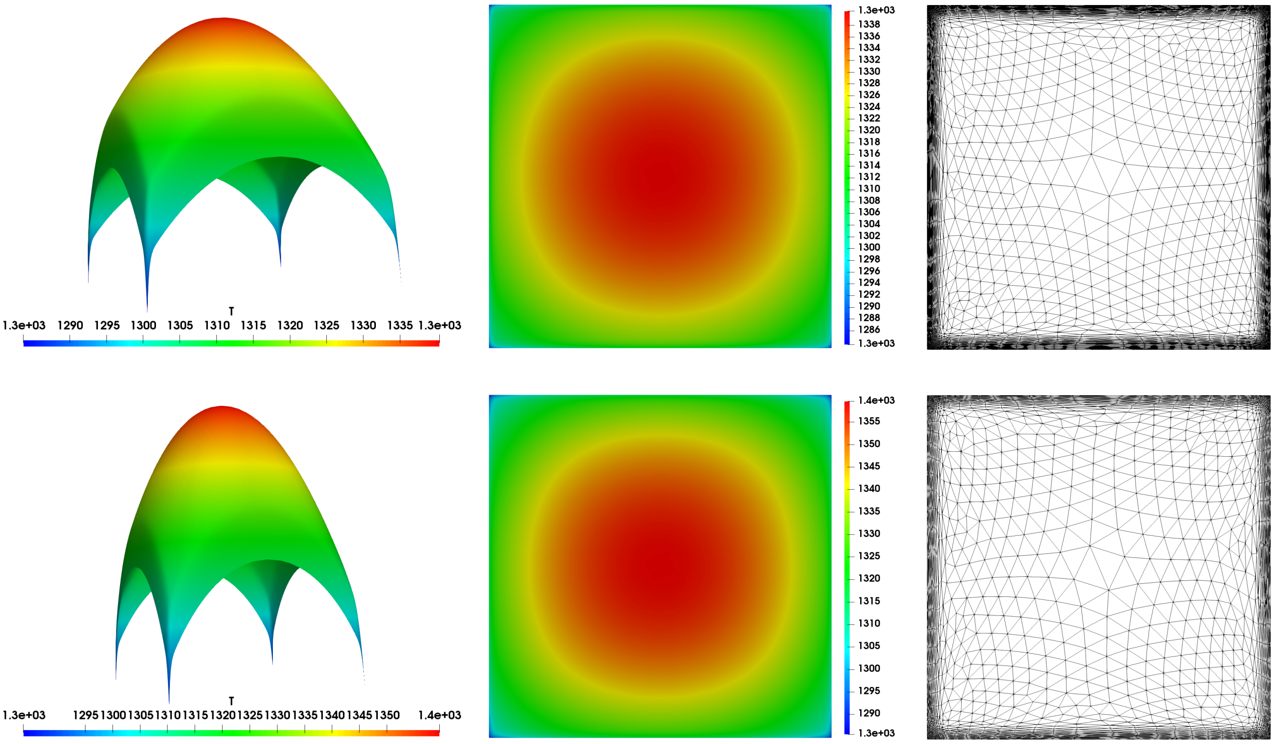

Figure 4.1: Temperature distribution (left), temperature snapshot (middle) and adapted mesh (right) obtained for the SP_1 approximation (first row) and the SP_3 approximation (second row) using $\varepsilon = 1$.

fixed time-step $\Delta t = 10^{-6}$ and the computed results are presented at the final time $T = 10^{-4}$. For solving the full radiative transfer equations in (2.1), we have implemented the well-established direct solver of Diffusion Synthetic Acceleration (DSA) method. This method has been widely used in computational radiative transfer as it accelerates the source iteration by using a diffusion approach. The reader is referred to [46, 36] for more details about the implementation of the DSA method. In our computations, the angle variable is discretized using the S_8 discrete-ordinate algorithm and we consider a structured uniform mesh of 100×100 grid-points resulting in linear systems of algebraic equations with 8×10^5 unknowns, which has to be solved at each timestep to calculate the mean radiative intensity.

In Figure 4.1 we present the plots of the temperature using two- and three-dimensional views along with the corresponding adapted meshes obtained for the SP_1 and SP_3 models using $\varepsilon = 1$. Those results obtained using $\varepsilon = 0.1$ are shown in Figure 4.2. A simple comparison of the temperature profiles in these figures reveals that a fast cooling is shown for the larger value of the diffusion scale $\varepsilon = 1$ while steeper thermal boundary layers are shown for the smaller value of $\varepsilon = 0.1$. These features are also reflected in the plots of the obtained adapted meshes for both SP_1 and SP_3 models at the considered asymptotic limits. A wider boundary band is detected at $\varepsilon = 1$ compared to the case using $\varepsilon = 0.1$ which is confined with the expected boundary layers for each optical regime in this radiative heat transfer problem. It is also clear that the anisotropic mesh adaptation performs well for this problem and captures the large thermal gradients in the considered raditive scales.

Next, we compare the results obtained using the SP_1 and SP_3 approximations with those obtained using the full radiative transfer. Figure 4.3 shows the 1D cross-sections at the main diagonal ($y = x$) of the temperature obtained with both values $\varepsilon = 1$ and $\varepsilon = 0.1$. It is evident that the proposed method for solving SP_1 and SP_3 models accurately capture the thermal boundary layers in this cooling problem. It is clearly presented that our adaptive method correctly solve the SP_3 model using both $\varepsilon = 1$ and $\varepsilon = 0.1$ and the results compare well with those obtained with the full radiative transfer equations using the DSA solver. In term of computational time, our adaptive method shows fast convergence compared to the DSA method. In fact, to solve the full radiative heat transfer problem, the direct DSA solver requires 793 and 1275 iterations to converge for $\varepsilon = 1$ and $\varepsilon = 0.1$,

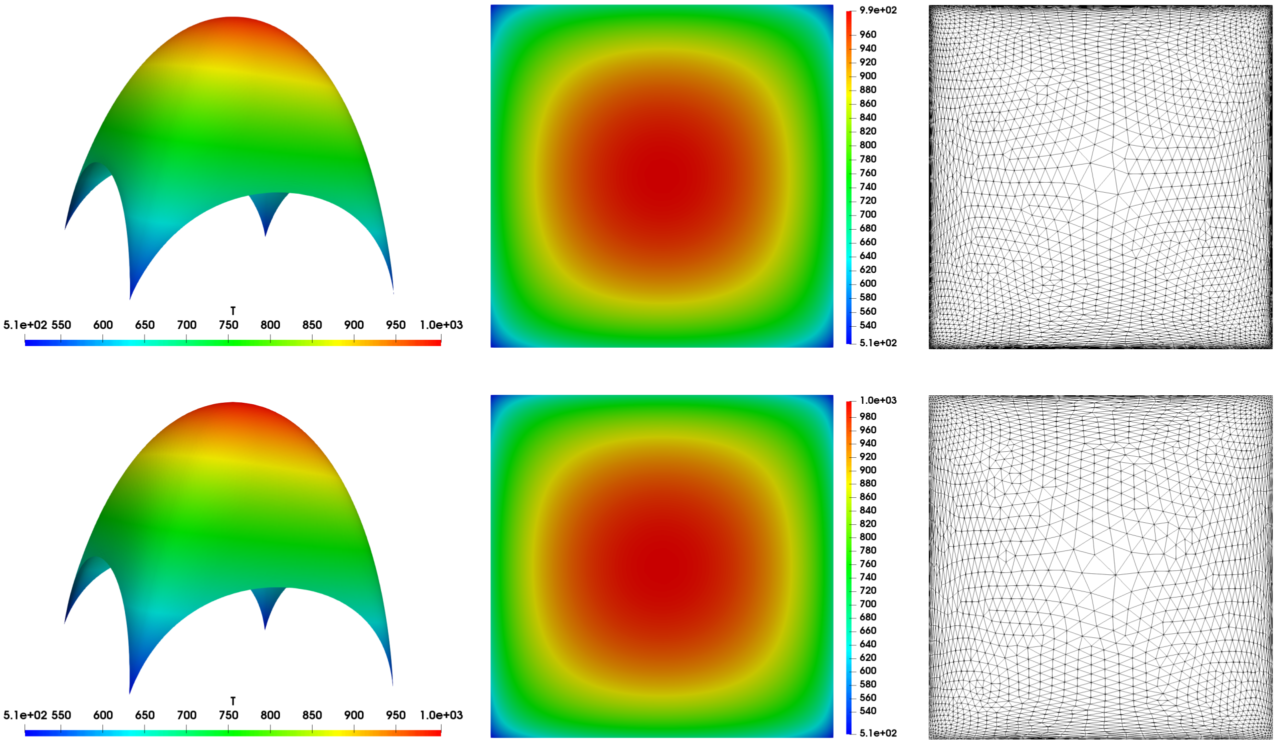

Figure 4.2: Same as Figure 4.1 but using $\varepsilon = 0.1$.

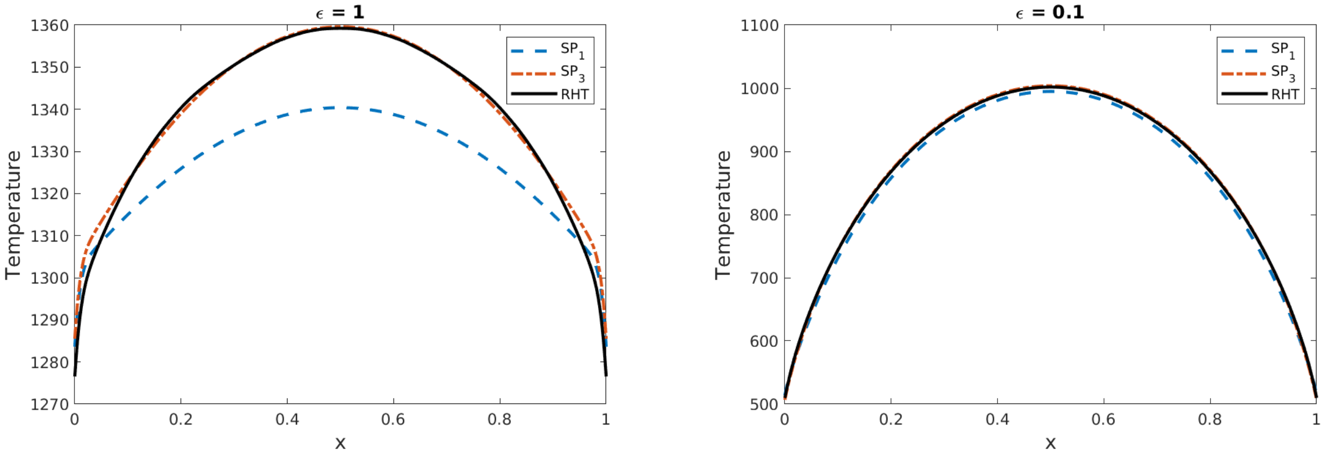

Figure 4.3: Comparison between the results obtained using the two-dimensional SP$_1$, SP$_3$ and full radiative heat transfer (RHT) models using $\varepsilon = 1$ (left) and $\varepsilon = 0.1$ (right).

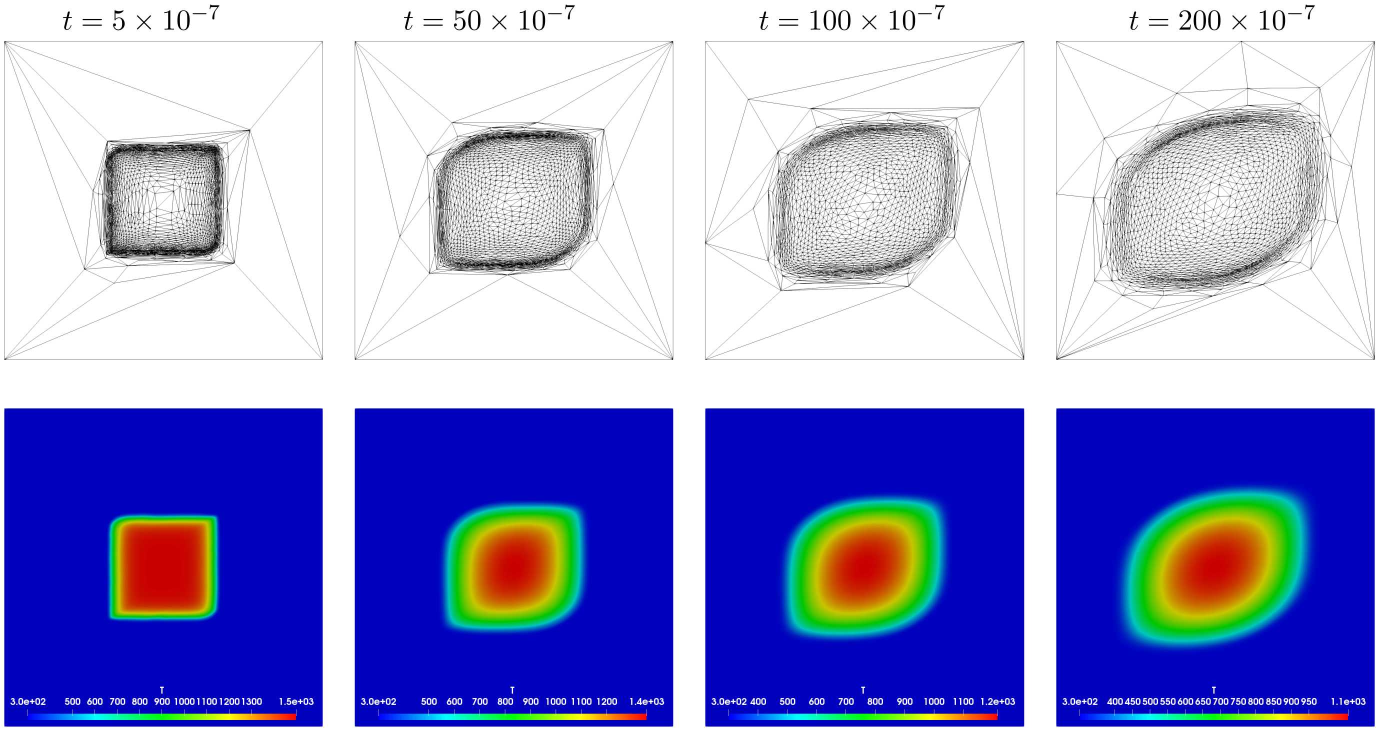

Figure 4.4: Adapted meshes (first row) and the corresponding temperature snapshots (second row) obtained with the SP$_3$ model using $\theta = \dfrac{\pi}{6}$ and $\varepsilon = 0.05$ at four different instants $t = 5 \times 10^{-7}$, 50×10^{-7}, 100×10^{-7} and 200×10^{-7}.

respectively. However, to solve the SP$_3$ model using the adaptive method with an average 3500 triangular elements shows fast convergence with a CPU time about 153 times lower compared to the full radiative model for a similar accuracy.

Our second example consists of a two-dimensional conduction-radiation problem in anisotropic media for which the governing equations are given by the SP$_3$ model (3.4). Note that based on the results obtained for the previous example, the SP$_3$ results are more accurate than the SP$_1$ results when compared to the full radiative heat transfer model results. Therefore, only results obtained using the SP$_3$ model are discussed for this example. The computational domain is the unit square $[0, 1] \times [0, 1]$ and the nonlinear conductivity is defined as

$$K_{11}(\Theta) = 0.1 + 0.02\Theta + 0.0005\Theta^2 \quad \text{and} \quad K_{22}(\Theta) = 0.1 + 0.02\Theta.$$

We also consider discontinuous absorption and scattering coefficients as

$$\sigma = \begin{cases} 0, & \text{if} \quad \Theta < 400, \\ 1, & \text{otherwise}. \end{cases} \qquad \kappa = \begin{cases} 10, & \text{if} \quad \Theta < 400, \\ 1, & \text{otherwise}. \end{cases}$$

The initial temperature is given by

$$\Theta_0(x, y) = \begin{cases} 1500, & \text{if} \quad (x, y) \in [0.35, 0.65] \times [0.35, 0.65], \\ 300, & \text{otherwise}. \end{cases}$$

The numerical simulations for this example are performed using a fixed time-step $\Delta t = 10^{-7}$ and the obtained results are presented in Figure 4.4. Here, we show time evolution of the temperature and the corresponding meshes for the asymptotic limit with $\varepsilon = 0.05$ and anisotropy with $\theta = \dfrac{\pi}{6}$. As it can be clearly

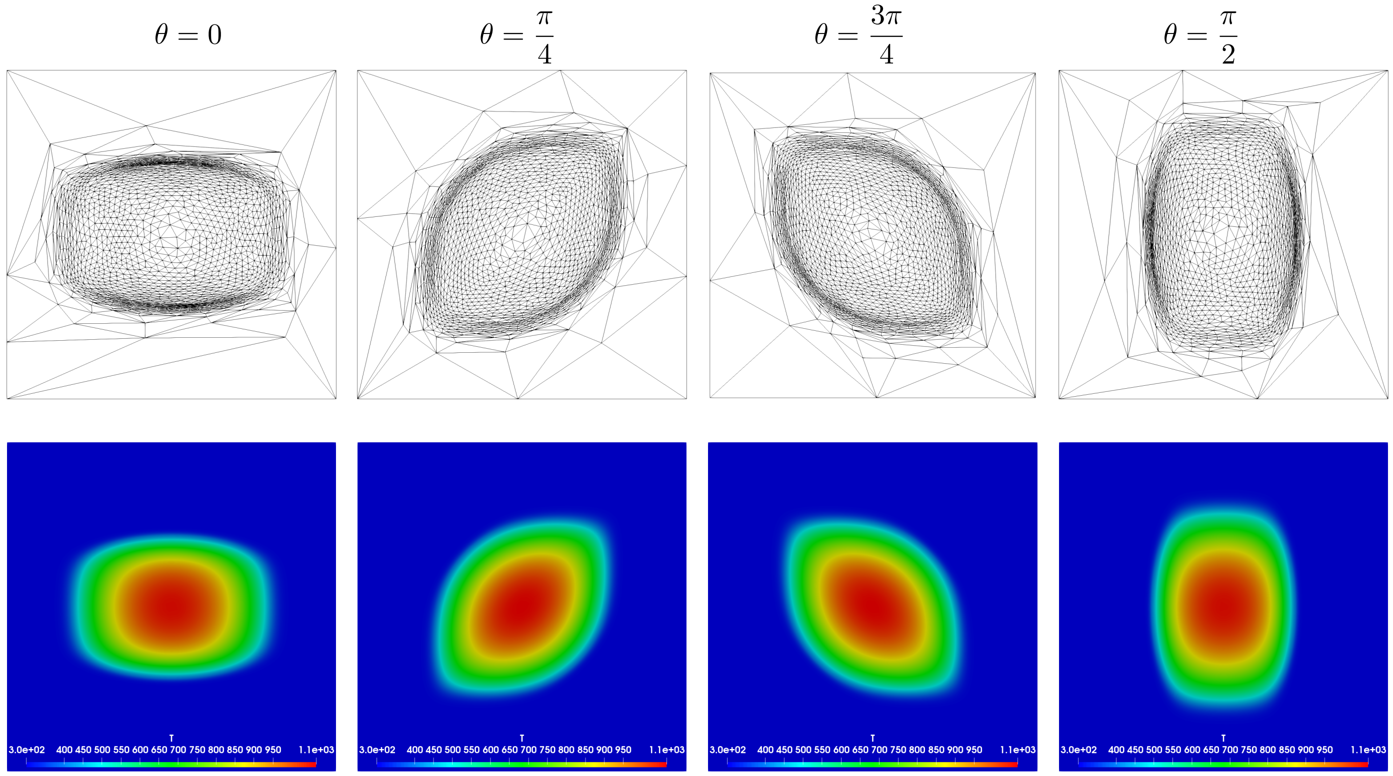

Figure 4.5: Adapted meshes (first row) and the corresponding temperature snapshots (second row) obtained with the SP$_3$ model at time $t = 2 \times 10^{-5}$ using $\varepsilon = 0.05$ and four different anisotropic angles $\theta = 0$, $\frac{\pi}{4}$, $\frac{3\pi}{4}$ and $\frac{\pi}{2}$.

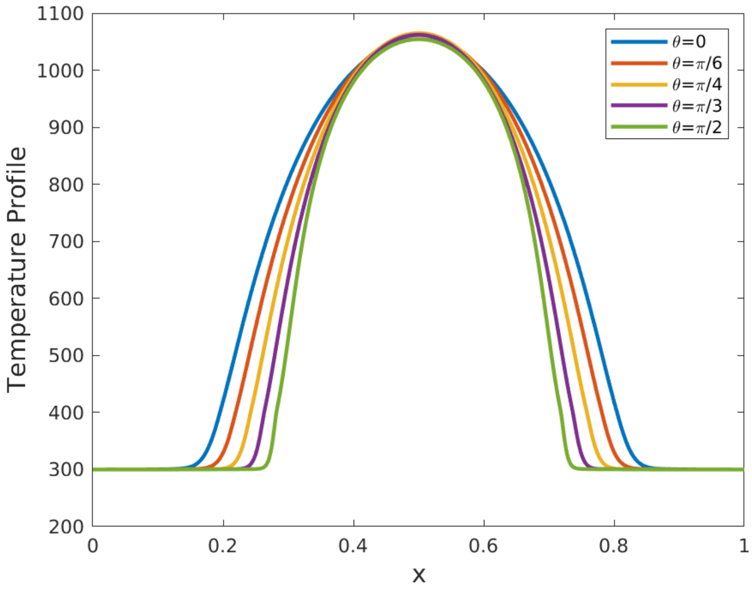

Figure 4.6: Cross-sections of the temperature along the horizontal centre line $y = 0.5$ for the two-dimensional anisotropic conduction-radiation problem at time $t = 2 \times 10^{-5}$ using $\varepsilon = 0.05$ and four different anisotropic angles $\theta = 0$, $\frac{\pi}{4}$, $\frac{3\pi}{4}$ and $\frac{\pi}{2}$.

Table 4.1: Mesh statistics, relative errors, and computational times for the SP$_3$ model on fixed uniform meshes using $\theta = \frac{\pi}{6}$ and $\varepsilon = 0.05$ at two different instants $t = 5 \times 10^{-6}$ and $t = 2 \times 10^{-5}$. The CPU times are per time-step and given in seconds.

		$t = 5 \times 10^{-6}$				$t = 2 \times 10^{-5}$			
Mesh	# Elem	E_Θ	E_ϕ	E_ψ	CPU	E_Θ	E_ϕ	E_ψ	CPU
1	5 000	3.75%	6.77%	6.67%	2.79 s	2.92%	7.39%	7.40%	2.79 s
2	20 000	0.86%	1.54%	1.51%	12.44 s	0.67%	1.63%	1.63%	12.44 s
3	80 000	0.36%	0.64%	0.64%	57.6 s	0.28%	0.69%	0.69%	57.6 s

Table 4.2: Same as Table 4.1 but on adaptive meshes.

		$t = 5 \times 10^{-6}$				$t = 2 \times 10^{-5}$			
Mesh	# Elem	E_Θ	E_ϕ	E_ψ	CPU	E_Θ	E_ϕ	E_ψ	CPU
1	3200	0.28%	0.59%	0.58%	28.17 s	0.20%	0.54%	0.55%	28.17 s
3	6300	0.10%	0.19%	0.18%	46.05 s	0.06%	0.14%	0.14%	46.05 s

seen, the meshes are refined in the vicinity of the front corresponding to $\Theta = 400$ where the absorption and scattering change the values providing highly accurate numerical solutions. This thermal front changes when the angle θ in (3.2) changes. This effect is clearly illustrated in Figure 4.5 where the temperature profile and the corresponding adapted mesh are depicted. To further demonstrate these features Figure 4.6 exhibits cross-section profiles of the temperature at $y = 0.5$ for different values of the angle θ. Decreasing the anisotropy angle θ results in a wider heat diffusion in these profiles of the temperature.

To demonstrate the performance of anisotropic mesh adaptation in comparison with fixed uniform meshes, quantitative results are also presented for this test example. Thus, the following discrete L^2-norm

$$E_u(n) = \frac{\left\|u^h(t_n) - u^{ref}(t_n)\right\|_2}{\left\|u^{ref}(t_n)\right\|_2} \times 100\%,$$

is used to compare the solutions obtained with uniform and adapted meshes, u^h, with a reference solution u^{ref} obtained on a fixed uniform fine mesh of 1280000 triangles. The results are presented in Table 4.1 and Table 4.2, where the computed E_u with the adapted and uniform meshes at time $t_n = 5 \times 10^{-6}$ and $t_n = 2 \times 10^{-5}$ are illustrated. These errors are computed using 5000, 20000 and 80000 for the fixed uniform meshes and using approximately 3100 and 5040 triangles for the adaptive meshes. These results in Table 4.1 and Table 4.2 clearly show the high accuracy of the adaptive meshes compared to the fixed uniform meshes. Here, the accuracy is clearly shown in terms of the L^2-norm, the CPU time and the significant gain in memory due the great reduction in the total number of triangles.

4.2 Radiative heat transfer in three-dimensional enclosures

To further examine the performance of the proposed method we consider two examples for radiative heat transfer in three-dimensional enclosures. In the first example we solve the the SP$_1$ model (2.5) and SP$_3$ model (2.6) in the unit cube $\mathcal{D} = [0, 1] \times [0, 1] \times [0, 1]$ of an isotropic medium with the heat conduction $\boldsymbol{K} = \mathbf{I}$, the

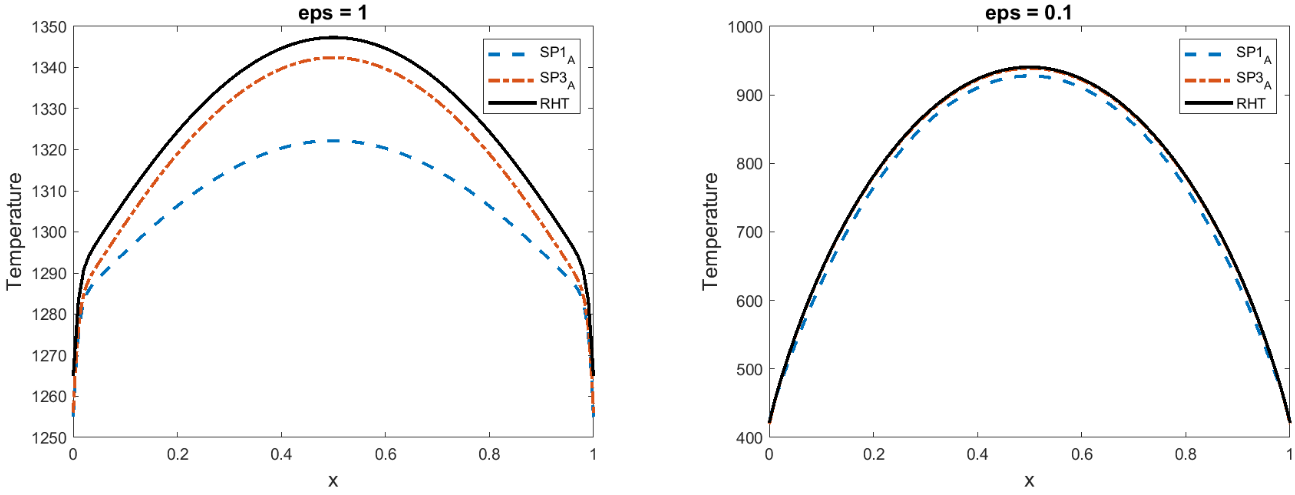

Figure 4.7: Comparison between the results obtained using the three-dimensional SP_1, SP_3 and RHT models using $\varepsilon = 1$ (left) and $\varepsilon = 0.1$ (right).

absorption coefficient $\kappa = 1$, the scattering coefficient $\sigma = 0$, the convective heat transfer coefficient $h_c = 1$ and the surface emissivity $\alpha = 0$. The initial and boundary temperatures are given as $\Theta_0 = 1500\ K$ and $\Theta_b = 300\ K$, respectively. As in the two-dimensional case, the numerical results obtained using the SP_1, SP_3, and RHT models are compared using two different optical regimes $\varepsilon = 1$ and $\varepsilon = 0.1$. The DSA method is also implemented to solve the three-dimensional RHT equations using $100 \times 100 \times 100$ grid-points for the discretization of the space variables and the S_8 discrete-ordinate algorithm for the discretization of the angle variable. In this case, linear systems of algebraic equations with 8×10^7 unknowns have to be solved at each time-step to calculate the mean radiative intensity. In Figure 4.7 we present cross-sections of the temperature profiles at the main diagonal obtained using SP_1, SP_3 and RHT models at time $t = 10^{-6}$. It is clear that for the considered asymptotic limits, the SP_1 and SP_3 models accurately capture the radiative features of the temperature.

It is also clear that our adaptive method correctly solves the SP_3 model using both $\varepsilon = 1$ and $\varepsilon = 0.1$ and the results compare very well with those obtained with the RHT model. Here as well, our adaptive method shows fast convergence compared to the DSA method. In fact, in our simulations for this example, to solve the RHT model with the DSA solver requires 587 and 1104 iterations to converge for $\varepsilon = 1$ and $\varepsilon = 0.1$, respectively. However, to solve the SP_3 model using the adaptive method demonstrates rapid convergence with a CPU time about 325 times lower compared to the RHT model for a similar accuracy.

Figure 4.8 shows the adapted meshes and temperature distributions obtained at time $t = 10^{-4}$ using the SP_3 model with $\varepsilon = 1$ for this example. As expected, steep boundary layers are present in the results which are automatically detected by our proposed adaptive method and thus finer elements were generated in the appropriate region. Similar results have been observed using $\varepsilon = 0.1$ for this test example but were not reported here to avoid repetition. As can be observed, the finite elements are concentrated only in the region where there is a stiff variation of the temperature allowing a great reduction in the total number of mesh tetrahedral elements and therefore reducing the computational resources. In the case with $\varepsilon = 1$ at time $t = 10^{-4}$, the total number of elements for the SP_3 model is 34500 resulting in linear systems of algebraic equations with only 149316 unknowns to be solved at each time-step. Thus, using the SP_3 model one can obtain numerical approximations as good as those obtained using the full radiation model, as shown in Figure 4.7, in only 8.5 min per time-step. This is due to both the use of the SP_3 model and the reduction of the total number of elements with the proposed adaptive mesh technique approximately 34500 tetrahedral elements. Therefore, one may conclude that using the proposed adaptive finite element method solving the SP_3 model performs well for this three-dimensional radiative heat transfer problem and resolves all the thermal features without the

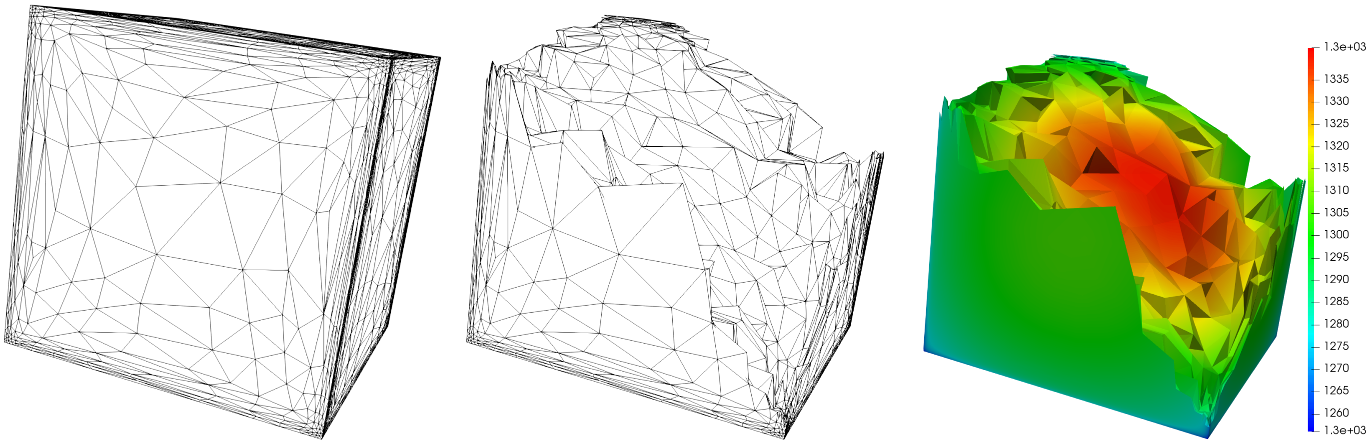

Figure 4.8: Adapted mesh and the temperature distribution obtained using the SP_3 model with $\varepsilon = 1$ for the radiative heat transfer problem in an cuboid enclosure.

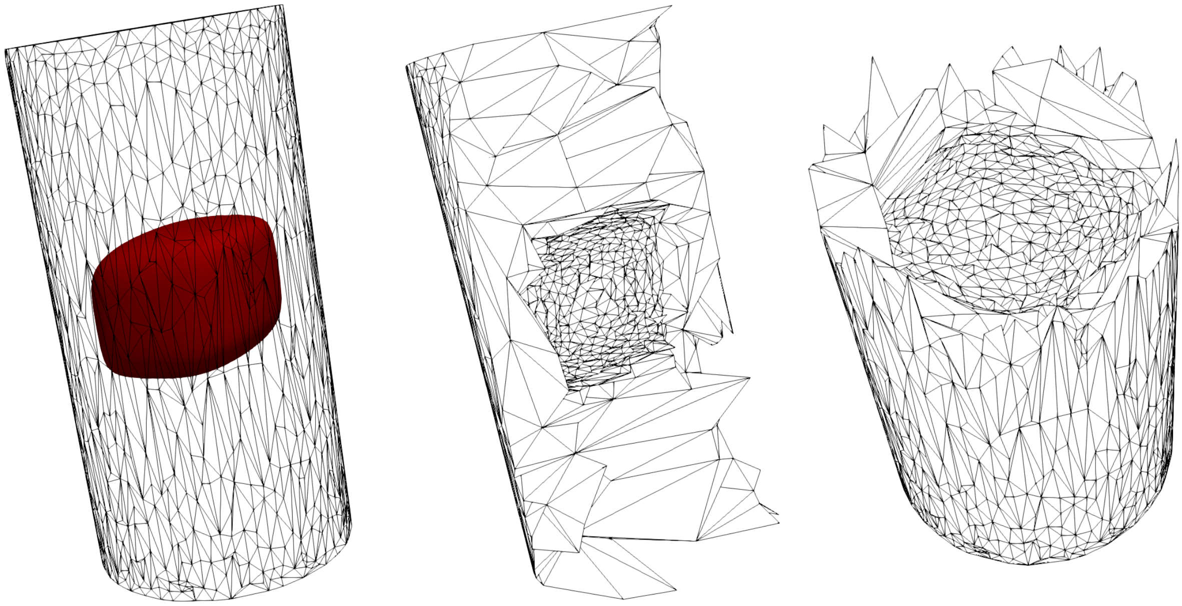

Figure 4.9: Adapted mesh and temperature distribution obtained using the SP_3 model with $\varepsilon = 0.05$ for the radiative heat transfer problem in an cylindrical. enclosure.

need for the full radiative heat transfer model (2.1) and extensive refined meshes. In addition, the results in this test example confirm our previous conclusions drawn for the two-dimensional about the efficiency of the proposed adaptive finite element method and show its ability in dealing with three-dimensional heat patterns on unstructured meshes.

Our final example consists of solving a three-dimensional problem of radiative heat transfer in anisotropic media. We consider a cylinder of 2 length and radius 0.5 with boundary temperature $\Theta_b = 300$ and initially

$$\Theta_0(x,y,z) = \begin{cases} 1300, & \text{on } \mathcal{D}_1 = [0.35, 0.65] \times [0.35, 0.65], \\ 300, & \text{otherwise.} \end{cases}$$

The absorption coefficient $\kappa = 1$, the scattering coefficient $\sigma = 0$, the convective heat transfer coefficient $h_c = 1$, the surface emissivity $\alpha = 0$ and the heat conduction $\boldsymbol{K}$ is assumed nonlinear with

$$K_{11}(\Theta) = 0.1 + 0.02\Theta + 0.0005\Theta^2, \qquad K_{22}(\Theta) = 0.1 + 0.02\Theta, \qquad K_{33}(\Theta) = K_{11}(\Theta).$$

The angle of anisotropy is set to $\theta = \frac{\pi}{3}$ and results are presented at time $t = 2 \times 10^{-5}$. In Figure 4.9 we display the obtained adaptive meshes along with the thermal front of $\Theta = 400\ K$ where the absorption and scattering coefficients change the values presented as a red surface in this figure. Note that it is expected to see localized internal and external boundary layers in the solution of this radiative heat transfer problem in anisotropic media due to the discontinuities in the initial temperature. As thinner thermal layers are considered, the present test example becomes more challenging to solve by the conventional finite element methods without mesh adaptivity. As it can be seen from the presented results, the meshes are refined in the vicinity of the front where the absorption and scattering change the values providing accurate numerical solutions with a total number of 32000 tetrahedral elements. It is worth remarking that the mesh orientation in Figure 4.9 is consistent with the anisotropy in the heat conduction tensor.

In summary, the adaptation procedure presented in this study gives encouraging results. Based on the results obtained for both two- and three-dimensional examples considered in the present work, it is clear that the error estimator accounting for the temperature distribution in the problem under study is suited for mesh adaptation in the finite element solution of radiative heat transfer equations.

5 Conclusions

We have presented an anisotropic mesh adaptation for nonlinear $\mathrm{SP_N}$ approximations of radiative heat transfer in both two- and three-dimensional enclosures. The thermal radiation has been approximated by the $\mathrm{SP_1}$ and $\mathrm{SP_3}$ models which are easy to be integrated in the finite element tools. We used a nonlinear coupling between the heat transfer and radiation for the $\mathrm{SP_N}$ equations in an anisotropic participating media. The proposed adaptive finite element method uses an efficient hierarchical error estimator appropriate for second- or high-order solutions. The performance of the proposed algorithms has been examined with several test problems including anisotropic radiative heat transfer in both two- and three-dimensional enclosures with discontinuous coefficients for different optical regimes. The obtained numerical results using $SP1$ and $SP3$ models showed a significant reduction in the computational cost compared to the results using the full radiative heat transfer model. The approach presented efficiently estimates the anisotropic temperature fields in radiative heat transfer problem. The proposed method can be applied to real world applications where there is a severe demand for efficiency in predicting the thermal radiation. Future work will focus on extending the proposed methodology to solve the coupled radiation and convection in non-gray participating anisotropic media. Parallel anisotropic mesh adaptation technique [47, 39] might also be suitable for this coupling, which will be subject of a future work. It will be also interesting to study the the coercivity, the existence and uniqueness of the presented model in this paper.

Acknowledgment. The authors wish to acknowledge the financial support provided by the Royal Society under the contract IES-R2-202078 and the financial support provided by the American University of Sharjah through Faculty Research Grant.

References

[1] M.F. Modest. *Radiative Heat Transfer.* Third edition. Academic Press, 2013.

[2] J.R. Howell, M.P. Menguc, and R. Siegel. *Thermal Radiation Heat Transfer.* Sixth edition. CRC Press, 2015.

[3] R. Viskanta. *Radiative Transfer in Combustion systems: Fundamental and Applications.* Begell House Publishers, 2005.

[4] S.T. Thynell. Discrete-ordinates method in radiative heat transfer. *International Journal of Engineering Science*, 36(12):1651–1675, 1998.

[5] S. Rosseland. *Theoretical Astrophysics: Atomic Theory and the Analysis of Stellar Atmospheres and Envelopes.* Clarendon Press, Oxford, 1936.

[6] M. Malek, N. Izem, M.S. Mohamed, M. Seaid, and M. Wakrim. Numerical solution of Rosseland model for transient thermal radiation in non-grey optically thick media using enriched basis functions. *Mathematics and Computers in Simulation*, 180:258–275, 2021.

[7] S.C. Ou and K.N. Liou. Generalization of the spherical harmonic method to radiative transfer in multi-dimensional space. *Journal of Quantitative Spectroscopy and Radiative Transfer*, 28(4):271–288, 1982.

[8] J. Yang and M.F. Modest. Elliptic pde formulation of general, three-dimensional high-order P_N-approximations for radiative transfer. *Journal of Quantitative Spectroscopy and Radiative Transfer*, 104(2):217–227, 2007.

[9] M.F. Modest and J. Yang. Elliptic pde formulation and boundary conditions of the spherical harmonics method of arbitrary order for general three-dimensional geometries. *Journal of Quantitative Spectroscopy and Radiative Transfer*, 109(9):1641–1666, 2008.

[10] E.M. Gelbard. Simplified spherical harmonics equations and their use in shielding problems. 1961. Technical Report WAPD-T-1182, Bettis Atomic Power Laboratory.

[11] E.W. Larsen, J.E. Morel, and J.M. McGhee. Asymptotic derivation of the multigroup p1 and simplified pn equations with anisotropic scattering. *Nuclear Science and Engineering*, 123(3):328–342, 1996.

[12] E.W. Larsen, G. Thömmes, A. Klar, M. Seaid, and T. Götz. Simplified P_N approximations to the equations of radiative heat transfer and applications. *Journal of Computational Physics*, 183(2):652–675, 2002.

[13] A. Klar, J. Lang, and M. Seaid. Adaptive solutions of SP_N-approximations to radiative heat transfer in glass. *International Journal of Thermal Sciences*, 44(11):1013–1023, 2005.

[14] M.S. Mohamed, M. Seaid, J. Trevelyan, and O. Laghrouche. Time-independent hybrid enrichment for finite element solution of transient conduction–radiation in diffusive grey media. *Journal of Computational Physics*, 251:81–101, 2013.

[15] M.S. Mohamed, M. Seaid, J. Trevelyan, and O. Laghrouche. An enriched finite element model with q-refinement for radiative boundary layers in glass cooling. *Journal of Computational Physics*, 258:718–737, 2014.

[16] Bruno Turcksin, Jean C. Ragusa, and Wolfgang Bangerth. Goal-oriented h-adaptivity for the multigroup SP_N equations. *Nuclear Science and Engineering*, 165(3):305–319, 2010.

[17] Jean C. Ragusa. Application of h-, p-, and hp-mesh adaptation techniques to the SP_N equations. *Transport Theory and Statistical Physics*, 39(2-4):234–254, 2010.

[18] S. Giani and M. Seaid. hp-adaptive discontinuous galerkin methods for simplified P_N approximations of frequency-dependent radiative transfer. *Computer Methods in Applied Mechanics and Engineering*, 301:52–79, 2016.

[19] C. Führer and G. Kanschat. A posteriori error control in radiative transfer. computing. *Computing*, 58:317–334, 1997.

[20] J.Patrick Jessee, Woodrow A. Fiveland, Louis H. Howell, Phillip Colella, and Richard B. Pember. An adaptive mesh refinement algorithm for the radiative transport equation. *Journal of Computational Physics*, 139(2):380–398, 1998.

[21] Y. Wang and J.C. Ragusa. Standard and goal-oriented adaptive mesh refinement applied to radiation transport on 2d unstructured triangular meshes. *Journal of Computational Physics*, 230(3):763–788, 2011.

[22] Y. Belhamadia and J. Grenier. Modeling and simulation of hypothermia effects on cardiac electrical dynamics. *PloS one*, 14(5):1–23, 2019.

[23] Y. Belhamadia, A. Fortin, and Y. Bourgault. On the performance of anisotropic mesh adaptation for scroll wave turbulence dynamics in reaction–diffusion systems. *Journal of Computational and Applied Mathematics*, 271:233–246, 2014.

[24] Y. Belhamadia, A. Fortin, and Y. Bourgault. Towards accurate numerical method for monodomain models using a realistic heart geometry. *Mathematical Biosciences*, 220(2):89–101, 2009.

[25] A. Fortin, T. Briffard, and A. Garon. A more efficient anisotropic mesh adaptation for the computation of Lagrangian coherent structures. *Journal of Computational Physics*, 285(0):100 – 110, 2015.

[26] F. Alauzet and A. Loseille. A decade of progress on anisotropic mesh adaptation for computational fluid dynamics. *Computer-Aided Design*, 72:13 – 39, 2016. 23rd International Meshing Roundtable Special Issue: Advances in Mesh Generation.

[27] H. Digonnet, T. Coupez, P. Laure, and L. Silva. Massively parallel anisotropic mesh adaptation. *The International Journal of High Performance Computing Applications*, 33(1):3–24, 2019.

[28] Y. Belhamadia, A. Fortin, and É. Chamberland. Anisotropic mesh adaptation for the solution of the Stefan problem. *Journal of Computational Physics*, 194(1):233–255, 2004.

[29] Y. Belhamadia, A. Fortin, and É. Chamberland. Three-dimensional anisotropic mesh adaptation for phase change problems. *Journal of Computational Physics*, 201(2):753–770, 2004.

[30] R. Viskanta and E.E. Anderson. Heat transfer in semitransparent solids. *Advances in Heat Transfer*, 11:317–441, 1975.

[31] Z Annasabi and F Erchiqui. 3d hybrid finite elements for anisotropic heat conduction in a multi-material with multiple orientations of the thermal conductivity tensors. *International Journal of Heat and Mass Transfer*, 158:119795, 2020.

[32] Yan Gu, Qingsong Hua, Chuanzeng Zhang, and Xiaoqiao He. The generalized finite difference method for long-time transient heat conduction in 3d anisotropic composite materials. *Applied Mathematical Modelling*, 71:316–330, 2019.

[33] R. Backofen, T. Bilz, A. Ribalta, and A. Voigt. SP_N-approximations of internal radiation in crystal growth of optical materials. *J. Crystal Growth.*, 266:264–270, 2004.

[34] M. Frank, M. Seaid, J. Janicka, A. Klar, R. Pinnau, and G. Thömmes. A comparison of approximate models for radiation in gas turbines. *Int. J. Progress in CFD*, 3:191–197, 2004.

[35] M. Seaid, A. Klar, and R. Pinnau. Numerical solvers for radiation and conduction in high temperature gas flows. *Flow, Turbulence and Combustion.*, 75:173–190, 2005.

[36] M. Seaid, M. Frank, A. Klar, R. Pinnau, and G. Thömmes. Efficient numerical methods for radiation in gas turbines. *J. Comp. Applied Math.*, 170:217–239, 2004.

[37] Y. Belhamadia. A time-dependent adaptive remeshing for electrical waves of the heart. *IEEE Transactions on Biomedical Engineering*, 55(2):443–452, 2008.

[38] Maryam Alqasemi and Youssef Belhamadia. A semi-implicit backward differentiation adi method for solving monodomain model. In *Computational Science – ICCS 2021*, pages 541–548, Cham, 2021. Springer International Publishing.

[39] Y. Belhamadia, T. Briffard, and A. Fortin. Efficiency of parallel anisotropic mesh adaptation for the solution of the bidomain model in cardiac tissue. *Journal of Computational Science.*

[40] Joseph M Powers. On the necessity of positive semi-definite conductivity and onsager reciprocity in modeling heat conduction in anisotropic media. *J. Heat Transfer*, 126(5):670–675, 2004.

[41] S. Balay, K. Buschelman, V. Eijkhout, W. Gropp, D. Kaushik, M. Knepley, L. C. McInnes, B. Smith, and H. Zhang. PETSc Users Manual. Technical Report ANL-95/11-Revision 2.1.6, Argonne National Laboratory, Argonne, Illinois, 2003.

[42] Y. Saad. *Iterative Methods for Sparse Linear Systems.* PWS Publishing Company, 1996.

[43] R. Bois, M. Fortin, and A. Fortin. A fully optimal anisotropic mesh adaptation method based on a hierarchical error estimator. *Computer Methods in Applied Mechanics and Engineering*, 209-212:12–27, 2012.

[44] T. Briffard. *Contributions à l'adaptation de maillages hiérarchiques.* PhD thesis, Département de mathématiques et de statistique, Université Laval, Québec, Canada, 12 2017.

[45] Y. Belhamadia, A. Fortin, and T. Briffard. A two-dimensional adaptive remeshing method for solving melting and solidification problems with convection. *Numerical Heat Transfer, Part A: Applications*, 76(4):179–197, 2019.

[46] M. Seaid and A. Klar. Efficient preconditioning of linear systems arising from the discretization of radiative transfer equation. *Lect. Notes. Comp. Sci.*, 35:211–236, 2003.

[47] Y. Belhamadia, T. Briffard, and A. Fortin. Application of parallel anisotropic mesh adaptation for solving monodomain cardiac model. *AIP Conference Proceedings*, 2343(1):130013, 2021.

Citation on deposit: Belhamadia, Y., & Seaid, M. (2023). Computing enhancement of the nonlinear SPN approximations of radiative heat transfer in participating material. Journal of Computational and Applied Mathematics, 434, Article 115342. https://doi.org/10.1016/j.cam.2023.115342